Originally published as:

Todd, M. C., Cavazos Guerra, C. (2016): Dust aerosol emission over the Sahara during summertime from Cloud-Aerosol Lidar with Orthogonal Polarization (CALIOP) observations. - *Atmospheric Environment*, *128*, p. 147-157.
DOI: http://doi.org/10.1016/j.atmosenv.2015.12.037

Atmospheric Environment 128 (2016) 147–157

Contents lists available at ScienceDirect

Atmospheric Environment

journal homepage: www.elsevier.com/locate/atmosenv

Dust aerosol emission over the Sahara during summertime from Cloud-Aerosol Lidar with Orthogonal Polarization (CALIOP) observations

Martin C. Todd [a, *], Carolina Cavazos-Guerra [b]

[a] Department of Geography, University of Sussex, Brighton, United Kingdom
[b] Institute for Advanced Sustainability Studies (IASS), Potsdam, Germany

HIGHLIGHTS

- Algorithm developed to identify active dust emission from CALIOP space borne Lidar data.
- Allows detection at night.
- Map of dust sources derived for the Sahara desert during the summer dust season.
- Shows strong convergence of evidence with previous independent analyses on preferential dust source regions.

ARTICLE INFO

Article history:
Received 23 December 2014
Received in revised form
13 November 2015
Accepted 15 December 2015
Available online 19 December 2015

Keywords:
Sahara
Dust
Aerosol
Preferential sources
CALIOP
Lidar

ABSTRACT

Dust aerosols are an important component of the climate system and a challenge to incorporate into weather and climate models. Information on the location and magnitude of dust emission remains a key information gap to inform model development. Inadequate surface observations ensure that satellite data remain the primary source of this information over extensive and remote desert regions. Here, we develop estimates of the relative magnitude of active dust emission over the Sahara desert based on data from the Cloud-Aerosol Lidar with Orthogonal Polarization (CALIOP). Utilising the unique vertical profile of aerosol characteristics provided by CALIOP our algorithm identifies emission from aerosol extinction and lidar backscatter in the near surface layers. From the long-term CALIOP archive of day and night-time orbits over 2006–13 we construct coarse resolution maps of a new dust emission index (DEI) for the Sahara desert during the peak summer dust season (June to September). The spatial structure of DEI indicates highest emission over a broad zone focused on the border regions of Southern Algeria, Northern Mali and northwest Niger, displaced substantially (~7°) to the east of the mean maximum in satellite-derived aerosol optical depth. In this region night-time emission exceeds that during the day. The DEI maps substantially corroborate recently derived dust source frequency count maps based on back-tracking plumes in high temporal resolution SEVIRI imagery. As such, a convergence of evidence from multiple satellite data sources using independent methods provides an increasingly robust picture of Saharan dust emission sources. Various caveats are considered. As such, quantitative estimates of dust emission may require a synergistic combined multi-sensor analysis.

1. Introduction

1.1. Dust source mapping from satellite

Atmospheric aerosols including mineral dust from deserts are an important component of the climate system by virtue of their direct radiative impacts, indirect effects on cloud properties, the semi-direct effect of these on atmospheric dynamics (Forster et al., 2007), and finally their role in global terrestrial and oceanic biogeochemical cycles e.g. (Jickells et al., 2005; Mahowald et al., 2010). Efforts to quantify these processes are at the cutting edge of climate science and their incorporation into Earth System Modelling remains a major challenge. Despite considerable

* Corresponding author.
E-mail address: m.todd@sussex.ac.uk (M.C. Todd).

http://dx.doi.org/10.1016/j.atmosenv.2015.12.037

progress in recent years models diverge very considerably in their estimates of emission at all scales (Textor et al., 2007; Todd et al., 2008).

The Sahara desert, the focus of this work is the world's primary source of dust aerosols. Dust is most extensive during the boreal summer when the vast expanse of the Central Western Sahara (CWS) exhibits the highest aerosols loadings observed anywhere on Earth, broadly co-located with the centre of the Saharan Heat Low (SHL) surface pressure minimum (Lavaysse et al., 2009) (Fig. 1). There is a high degree of uncertainty in the spatial pattern of mineral dust emission over the Sahara in the current generation of climate models contributing to the IPCC assessment Report 5 (Fig. 2a) and a poor agreement in mean Aerosol Optical Thickness (AOT) between models and satellite observations (compare Fig. 2b and Fig. 1). This uncertainty highlights the need for accurate maps of dust emission for the Sahara to inform model development.

Satellite observations remain the most potent source of information on dust source regions. Global dust sources have been inferred from sensors providing daytime observations of Aerosol Index (AI) from the Total Ozone Mapping Spectrometer (TOMS) (Chiapello and Moulin, 2002; Prospero et al., 2002; Washington et al., 2003) and AOT from various sensors including the Moderate Resolution Imaging Spectroradiometer (MODIS), the Ozone Monitoring Instrument (OMI) and the Multi-angle Imaging Spectroradiometer (MISR) amongst others. These source region maps have helped improve aerosol modules in models (Ginoux et al., 2001; Tegen et al., 2002).

However, inferring the actual dust sources from fields of AOT/AI from such polar-orbiting satellite is problematic. First, there are inconsistencies in dust loading estimates between sensors, which can lead to markedly differing inferences of source regions (Banks et al., 2013; Schepanski et al., 2012). Second, AI/AOT is a column-integrated quantity such that observations reflect both aged dust and any recently emitted plumes. Third, optical sensor's daytime only observations leads to substantial biases in mean AOT estimates (Kocha et al., 2013). The Infrared Atmospheric Sounder Interferometer (IASI) can provide infrared AOT estimates at night e.g. (Peyridieu et al., 2013) but lacks sensitivity to dust in the boundary layer.

To account for this, at least over the Sahara desert, methods have been developed which utilise the high 15-min temporal resolution afforded by imagery from the Spinning and Enhanced Visible and Infrared Imager (SEVIRI) sensor on the geostationary Meteosat Second Generation (MSG) satellite. Dust plumes are identified using the SEVIRI thermal infrared-based false colour dust product (Lensky and Rosenfeld, 2008) and then 'back-tracked' to their source regions, either manually (Schepanski et al., 2007), (hereafter S07) or automatically, at very high resolution (Ashpole and Washington, 2012, 2013b) (hereafter AW13), allowing the derivation of 'dust source activation' (DSA) frequency over many years of data. These maps of DSA differ markedly from those of column dust AI or AOT in that the former (Fig. 3a,b) highlight specific sources within the wider regions of high average column-integrated AOT (Fig. 1). As such, the SEVIRI DSA maps have substantially enhanced our understanding of dust sources and meteorological emission patterns and processes (e.g. Schepanski et al., 2009).

Nevertheless, SEVIRI DSA method has a number of potential limitations. (i) It assumes dust plumes are emitted from a discrete single source with minimal further emission during propagation away from that initial source. This may not be valid in some cases (as illustrated in Section 3 below). (ii) Dust plume detection capability is weaker at night, leading to an un-quantified diurnal bias,

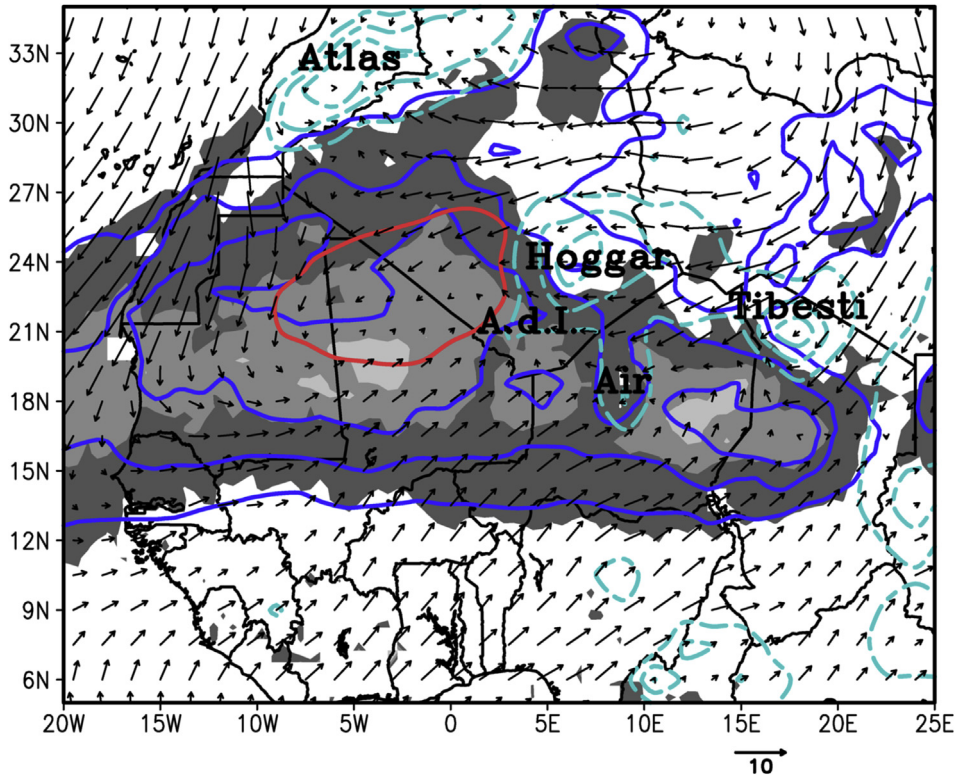

Fig. 1. Dust distribution over the Sahara during June–September. Mean MISR AOT 2000–12 (shaded, contours from 0.4 at 0.2 intervals), mean TOMS AI 1983–2001 (blue contours at 0.2–0.6, with interval 0.2). Also shown are the atmospheric circulation fields of 925 hPa winds and position of the SHL indicated by the 1000 hPa mean sea level pressure contour (red contour) from ERA-Interim data (1979–2012). Surface topography is also presented (cyan dashed contours 1000–2000 m with 500 m interval) and major mountain ranges are labelled ('A. d. I.' refers to the Adrar des Ifoghas range). (For interpretation of the references to colour in this figure legend, the reader is referred to the web version of this article.)

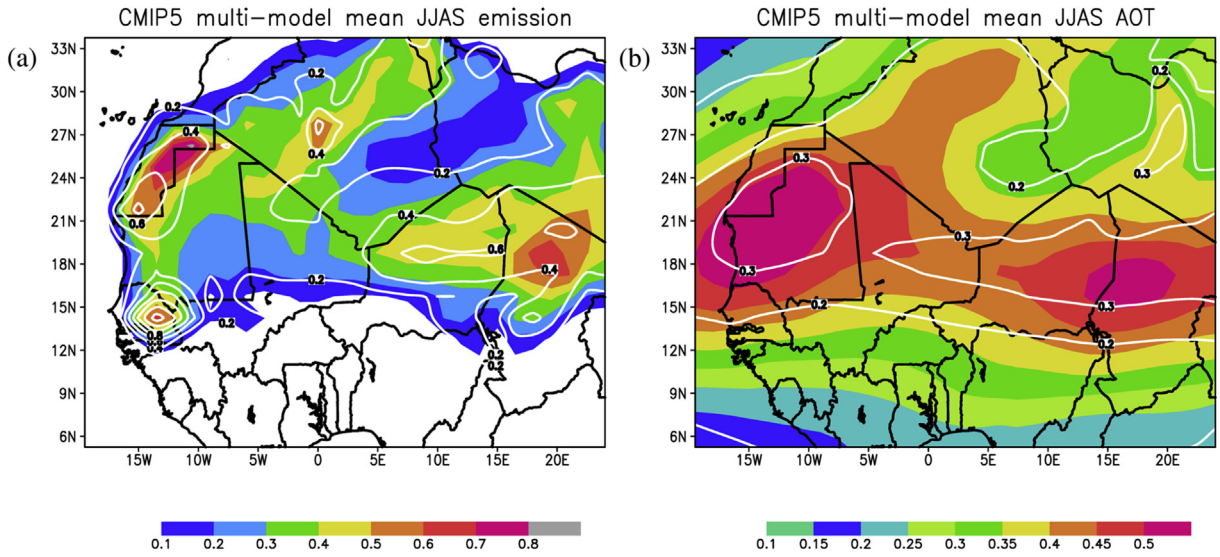

Fig. 2. Multi-model mean June–Sept dust emission (g m^{-2} day^{-1} shaded) and inter-model standard deviation (contours) from 14 global models contributing to the fifth Coupled Model Intercomparison Project (CMIP5) for the period 1970–2000 under the historical simulation (see (Evan et al., 2015) for list of models) (b) As (a) but for dust AOT from 22 models (models as (Evan et al., 2015) and in addition ACCESS1-3, BNU-ESM, CESM1-CAM5, GFDL-ESM2G, GFDL-ESM2M, IPSL-CM5A-LR, IPSL-CM5A-MR, IPSL-CM5B-LR, NorESM1-ME).

and in moist atmospheres where water vapour absorption is pronounced (Ashpole and Washington, 2012; Brindley et al., 2012). (iii) DSA is a count of dust plume emission and may not equate simply to the magnitude of emission from identified sources. (iv) DSA frequencies have not been normalised for spatial sample size variability associated with cloud cover.

In this paper we contribute to this growing understanding of dust sources through development of a method to identify and quantify dust emission from aerosol vertical profiles from the Cloud-Aerosol Lidar with Orthogonal Polarization (CALIOP) instrument on board the Cloud-Aerosol Lidar and Infrared Pathfinder Satellite Observation (CALIPSO) satellite.

1.2. Dust emission from the Sahara desert during summer

Two characteristics of the CWS dust are of particular importance to this study. First, the prevalence of aged dust mixed throughout the deep Saharan boundary layer within the SHL can hinder identification of sources: i.e. broad extent of high AOT (Fig. 1) and localised DSA (Fig. 3). This is a prime motivation for the use of vertical profiling information in this study. Second, night-time emission is prevalent over the Sahara in summer generated by high winds from nocturnal mesoscale 'cold pool' density currents (producing the '*haboob*' dust events) associated with Mesoscale Convective Systems (MCS) e.g. (Allen et al., 2013; Emmel et al., 2010; Flamant et al., 2009; Knippertz and Todd, 2010; Marsham et al., 2013; Williams et al., 2009). Identification of night-time emission is a problem for all existing satellite methods. In addition to *haboobs*, synoptic-scale surface wind events drive dust emission, and include both northerly Harmattan wind surges and southerly monsoon surges around the SHL. In these events dust emissions typically peak in the mid-morning when the nocturnal low level jets (LLJs) are mixed to the surface in the growing daytime boundary layer (Fiedler et al., 2013; Marsham et al., 2013; Schepanski et al., 2009; Todd et al., 2013; Washington et al., 2006).

In this paper we provide a method to identify active emission from CALIOP, during day and night, over the CWS dust region during summer, and to accumulate statistics to derive the spatial distribution of a Dust Emission Index (DEI). We use this vertical profile information to identify and quantify active dust emission near the ground surface.

2. Data and methods

CALIOP measures vertical profiles of aerosol backscatter (BS) and extinction coefficient (EC) at 532 and 1064 nm, respectively night and day (at ~01:30 and 13:30 local time) (Vaughan et al., 2004; Winker et al., 2009; Young and Vaughan, 2009). The official algorithms developed for both cloud/aerosol layer identification and discrimination are described in full in (Liu et al., 2009; Winker et al., 2009). As a nadir-viewing profiling instrument with very narrow swath CALIOP has relatively poor temporal resolution with a revisit time period of ~16 days. Nevertheless, the dataset extends from June 2006 to present providing sufficient sampling for robust characterisation of aerosol distribution in 3 dimensions (Ridley et al., 2012; Winker et al., 2010).

We use the latest versions of the level-2 (L2) products (Versions 3.01, 3.02 and 3.03 depending on date), which have improvements in cloud-aerosol discrimination and layer-base determination for boundary layer aerosols (Liu et al., 2009). In the description below we refer to each orbit as a data 'curtain', given the very narrow width of the lidar beam, providing an along-track 2-D latitude-height data matrix with 60 m vertical and 5 km horizontal resolution.

2.1. CALIOP data quality control screening and processing

Prior to application of the emission detection algorithm (Section 2.2) a comprehensive quality control and cloud/dust screening procedure was applied. (i) Screening out L2 data samples with low feature classification confidence (Winker et al., 2013). The Atmospheric Volume Description flag must be equal to 0; the cloud-aerosol discrimination (CAD) Score must be in the range −20 to −100; the Extinction Quality Control must be equal to 0, 1, 2, 16 or 18; the extinction coefficient uncertainty must be less than 10 km^{-1}. (ii) Identifying and correcting CALIOP misclassification of thick dust as cloud, documented previously (Chen et al., 2010) and noted in analysis of test cases of known dust events here. All

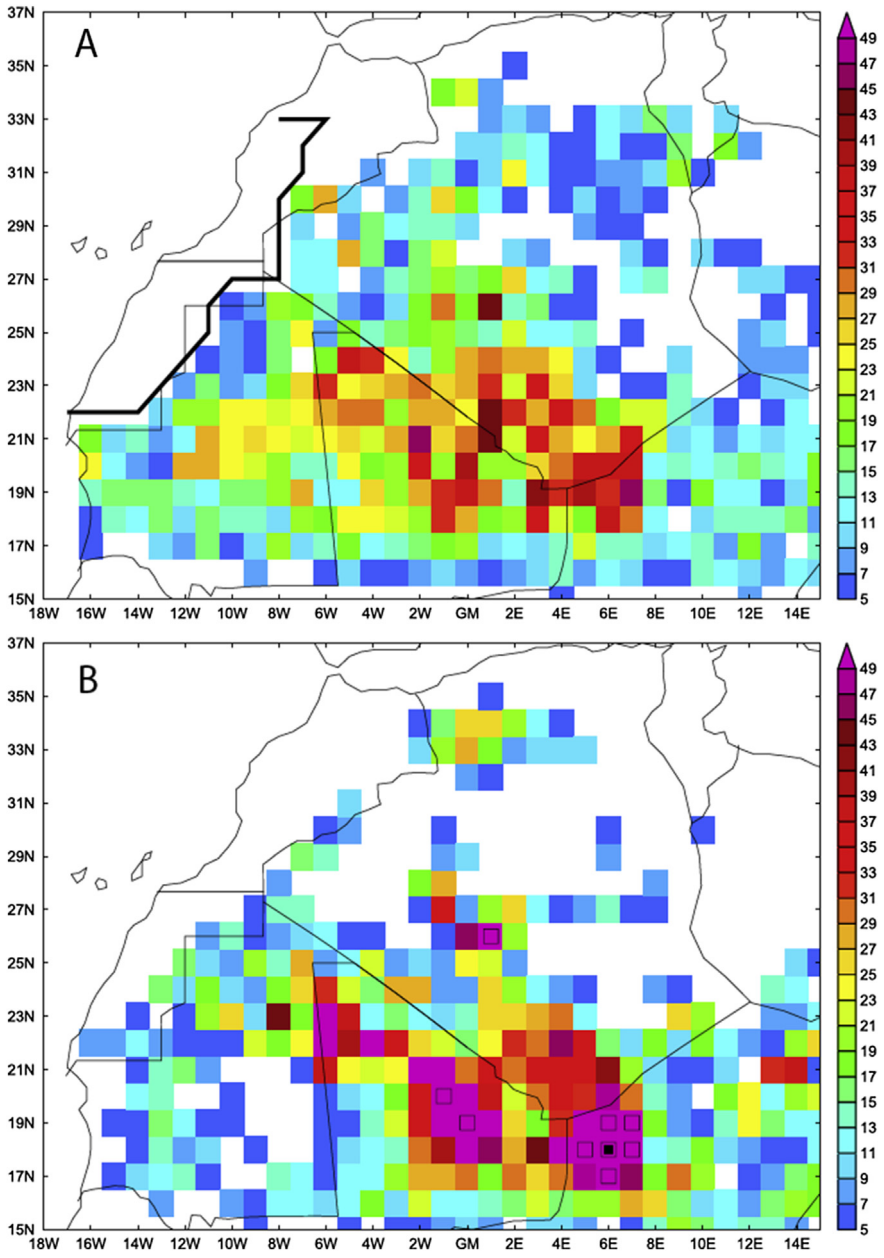

Fig. 3. Dust source activation (DSA) frequency from SEVIRI aggregated to 1° resolution for comparative purposes for 2006–2009 June–August inclusive derived by AW13 using the method of (a) AW13 (original data is at 0.03° resolution) (b) S07. White regions correspond to DSA < 5, and black outlined (filled) boxes on (b) correspond to count ≥ 60 (90). Black outline on (a) highlights the masked region where source detection is set to zero by AW13 (adapted from AW13 Fig. 7).

misclassified cloud was reclassified as aerosol where aerosol subtype information is available, the cloud is over a desert surface north of 17°N, and the top of the misclassified cloud is below 1500 m height. (iii) Screening out cloud-contaminated profiles in which total attenuation of the lidar beam by cloud prevents sampling of dust layers below. A count of the number of remaining valid profiles is accumulated so that the final dust emission quantities can be scaled by the cloud-free sampling frequency. (iv) Screening out all non-dust aerosol cells. Only data points classified as dust from the CALIOP feature classification (and misclassified cloud) are retained for analysis of emission. Note that total attenuation of the lidar beam can occur with high AOT > ~4, preventing EC retrieval in the near surface layers. Such cases are necessarily screened out and constitute an unavoidable bias in the emission estimation method. (v) Noise reduction filtering. The screened data curtains of EC and BS are then filtered using a 9 × 5 pixel median filter to reduce 'salt and pepper' noise characteristic of CALIOP data especially during daytime.

2.2. Identification of active dust emission events

Those individual CALIOP profiles with active dust emission are identified based on the premise that emission is characterised by a vertical profile of dust EC values in which there is, in the lowest layers immediately above the surface (i) a local EC maximum of sufficient magnitude to distinguish emission events from background EC values (ii) a pronounced negative EC gradient with height to distinguish active dust emission from aged dust subjected to extensive vertical mixing. Threshold values of near surface EC and vertical gradient of EC are defined from careful analysis of a

large number of known dust events observed during 2010 and 2011 including the period of coincident with the 'Fennec: The Saharan Climate System' project observation period (see Marsham et al., 2013). For these dust emission profiles EC is then integrated over the depth of the dust emission layer to provide the DEI. We tested a wide range of threshold values for all the parameters in steps 1–3 described below in a comprehensive sensitivity analysis. We find low sensitivity in the spatial structure of DEI to parameter values over ranges of at least a factor of 5, as indicated by DEI pattern correlations above 0.9.

In the description below we illustrate each algorithm step with a real example of a '*haboob*' convective cold pool event (Fig. 4) described in more detail in Section 3. In this case active dust emission is evident in SEVIRI imagery (Fig. 4a, Feature A) and the vertical profile of EC within the *haboob* leading edge (black line in Fig. 4d) indicates a dust layer of about 1 km in depth.

Step 1Identification of discrete dust layers.

For each individual vertical profile in the data curtain discrete dust layers are identified from break-points (changes) in the sign of the local vertical EC gradient, δEC, where δEC exceeds a threshold of 0.025 km^{-1}. The value of this threshold was established to ensure a reasonable number of discrete layers (typically a maximum of 5) consistent with the characteristics of vertical dust distribution during Fennec (Ryder et al., 2013). Then, for the dust layer nearest the surface, a number of metrics are derived; (i) The maximum EC (EC_{max}) and BS (BS_{max}) within the layer. (ii) The height, h, above the surface of the layer of EC_{max}. (iii) The height of the top of the dust layer (h_{top}) defined as the height of the δEC break point above height h. For illustration see Fig. 4d.

Step 2Dust emission identification.

An individual profile is flagged as a dust emission event when it contains a dust layer located immediately above the desert surface (h < 500 m a.g.l.) of sufficient magnitude (EC_{max} > 0.25 km^{-1}) and vertical gradient, (where EC declines to <50% of EC_{max} between height h and h_{top}) (see Fig. 4d for illustration). In addition, further dust emission events are flagged where the L2 feature misclassification errors described in Section 2.1 (ii) are identified. The EC_{max} threshold of 0.25 km^{-1} is ~25% of the typical value for moderate dust events ensuring that small events are captured whilst minimising spurious false alarms from data noise. We minimise this risk further by applying a further condition that BS_{max} > 0.025 sr^{-1}. Very small-scale dust emission not captured by the EC_{max} and BS_{max} thresholds likely contribute only marginally to total emission (Allen et al., 2013). The threshold value of h (500 m a.g.l.) is consistent with the characteristics of known dust events studied during the Fennec project. Night-time (often *haboob* type) dust plumes are typically below ~800 m a.g.l. (Allen et al., 2013; Marsham et al., 2013). For daytime synoptic-scale wind events at the time of peak emission, typically in the morning, the dust layer is typically <600 m a.g.l., and although subsequently mixed vertically through to ~1 to 2 km height in the PBL by the early afternoon time of the CALIOP pass, the maximum dust concentration peaks towards the surface (Marsham et al., 2013). Thus, a threshold h value of 500 m a.g.l. is physically reasonable, ensuring that EC_{max} must occur below the approximate midpoint height of a typical dust emission plume.

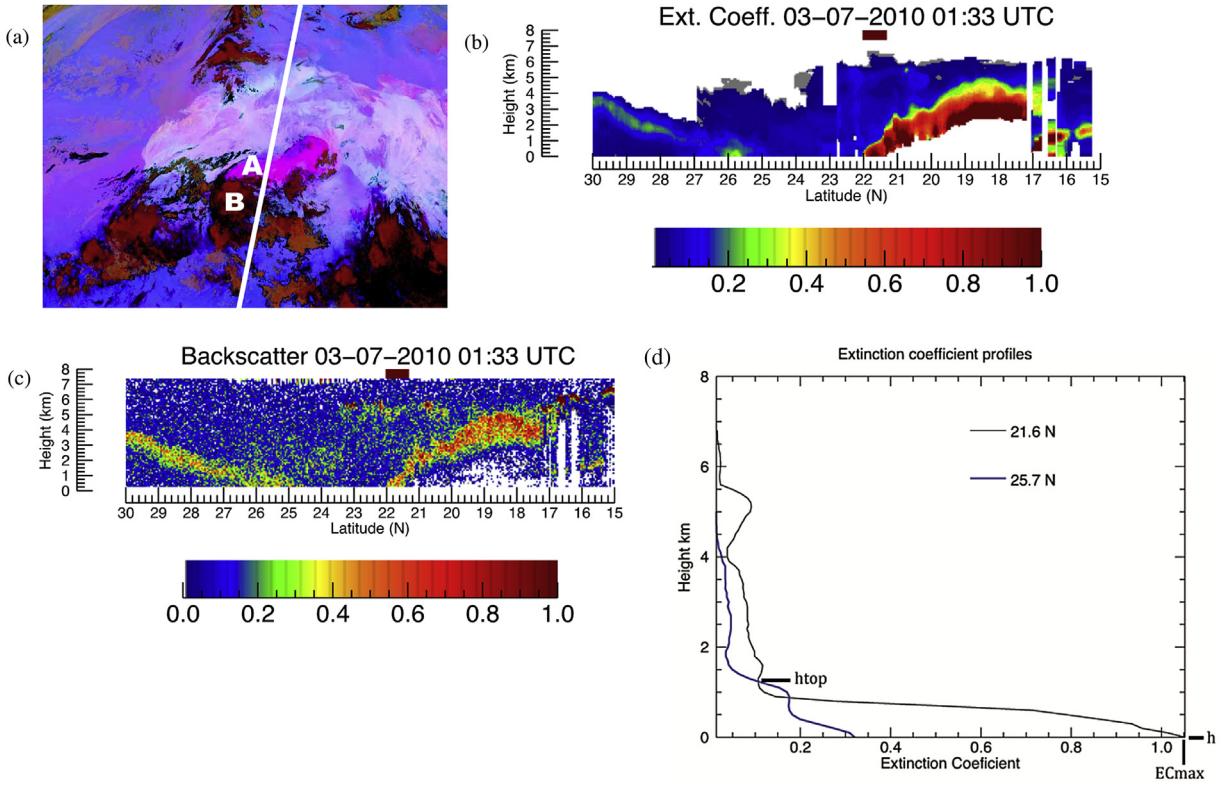

Fig. 4. Illustrative example of the dust emission algorithm over North Africa, at 01.30 UTC on 3rd July 2010. (a) SEVIRI false colour dust product, with the approximate location of the CALIOP orbit shown by the thick white line (see text for explanation of other annotation). Dust plumes appear in pink tones, clouds as dark red-black. (b) CALIOP latitude-height data curtain of 532 nm extinction coefficient (km^{-1}, after quality control processing, screening and noise filtering). Horizontal bars in brown above image indicate profiles flagged as active dust emission. (c) As (b) but for 1064 nm total attenuated backscatter (km^{-1} sr^{-1}). (d) Individual vertical profiles of 523 nm extinction coefficient (km^{-1}) at selected latitude points (see text for explanation of marked variables). (For interpretation of the references to colour in this figure legend, the reader is referred to the web version of this article.)

Step 3Derive dust emission index (DEI).

For profiles flagged with active emission the total EC in the dust emission layer (the DEI) is calculated by integrating EC from the surface to h_{top}. Therefore, the estimate of DEI should account for all dust emitted and then mixed vertically and is considered here to be a proxy of the dust mass in the dust layer.

Step 4 Space/time aggregation.

All the derived emission metrics are binned into a gridded map at 1.5° resolution to ensure adequate sample sizes from the CALIOP data. The mean DEI in each 1.5° grid cell is the sum of all DEI values over the entire record June–September 2006–13, scaled by the total number of cloud attenuation-free observations contributing to that 1.5° grid cell, thereby correcting for the spatial distribution of cloud-obscured data. Mean DEI is also disaggregated for day and night CALIOP passes. With low temporal sampling (CALIOP has a 16-day repeat cycle) the total number of samples per 1.5° grid cell per summer season obtained is lower than (by about 2–4 times) that of other sensors with daily or (lower temporal sampling) such as TOMS and MISR.

3. Case study examples of dust event detection

To illustrate the algorithm performance we present a set of cases representative of the major meteorological conditions driving dust emission (Figs. 4–7). In the case of the 3rd July 2010 (Fig. 4) active dust emission associated with a *haboob* convective cold pool (Feature A in Fig. 4a) spread northwards from a convective cloud system (Feature B) over northwest Niger. The 'nose' of the *haboob* dust emission front is evident in CALIOP (Fig. 4b,c) at ~21.5°N, 4°E, as a southward slanting BS and EC profile, as the cool, moist cold pool undercuts the hot dry Saharan air to the North. The algorithm clearly identifies active emission from high EC in the near surface layers at the *haboob* leading edge (brown block above EC profile in Fig. 4b). The vertical profile of EC within the *haboob* leading edge indicates a dust layer of about 1 km in depth (black line in Fig. 4d) clearly distinguishable from the cleaner air to the North (blue line). To the south of the active emission a deep dust layer up to ~5 km height a.g.l., apparent from the EC and BS profiles (Fig. 4b,c) extends from ~17° to 20°N. This is aged dust emitted on the previous night and subsequently mixed throughout the Saharan residual layer (this dust layer is sufficiently thick to cause total attenuation of the lidar beam). As such, the algorithm is able to distinguish active dust emission from aged dust.

A further cold pool event occurred on 21st June 2011 in which the *haboob* (Feature A in Fig. 5a) was generated from nocturnal convection (Feature B in Fig. 5a) over the Atlas Mountains of Northern Morocco and Algeria, and propagated southward into the North-western Sahara. The northward slanting *haboob* nose evident in the CALIOP EC and BS data at ~26.5°N (Fig. 5b,c). Dust emission within the *haboob* front is identified by the algorithm (Fig. 5b and black line Fig. 5d). Active emission is clearly distinguished from the elevated dust layer behind the nose to the North (blue line in Fig. 5d) where emitted dust is lofted, and from the background low aerosol loadings to the south (red line Fig. 5d).

A case of emission within the nocturnal monsoon flow on 28th June 2010 is presented in Fig. 6. In this case an extensive area of high dust loadings is evident over much of Northern Niger and Southern Algeria (Fig. 6a) resulting from repeated and intense *haboob* events in the region over the previous 3 days. Within this, our algorithm (Fig. 6b,c) is able to identify active emission at ~16°N which we assume is associated with turbulence in the nocturnal

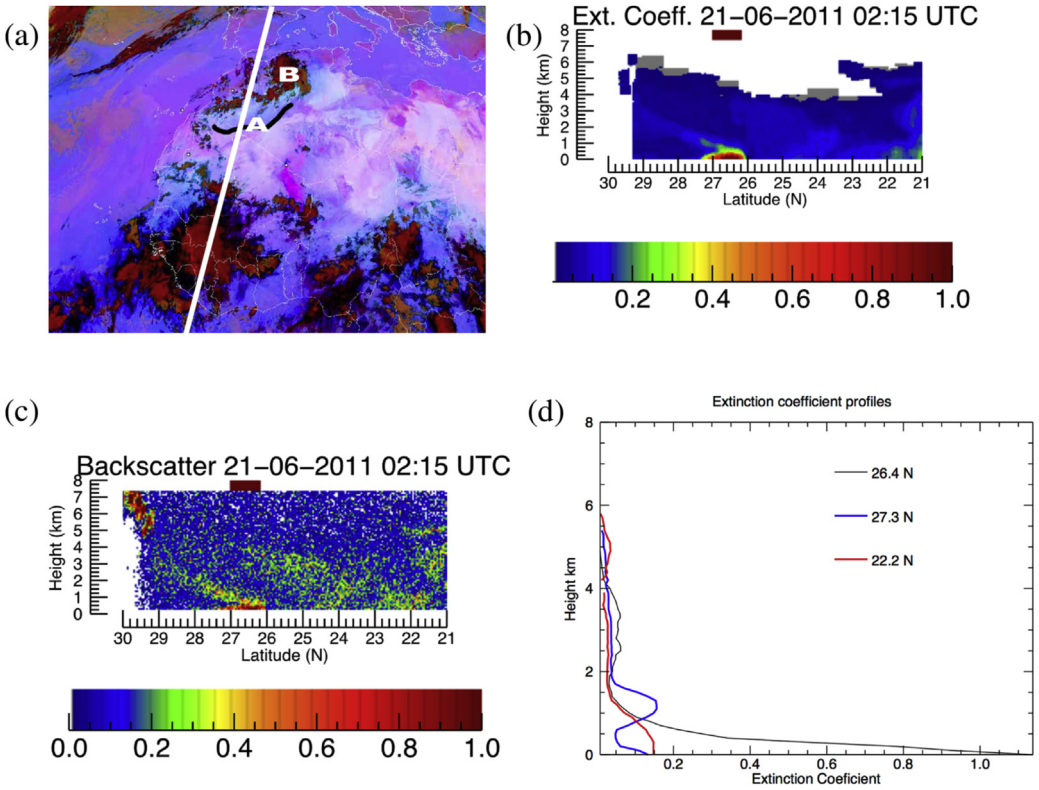

Fig. 5. As Fig. 4 but for 21st June 2011 at 02.15UTC. The black line marks the approximate position of the advancing nose of the haboob.

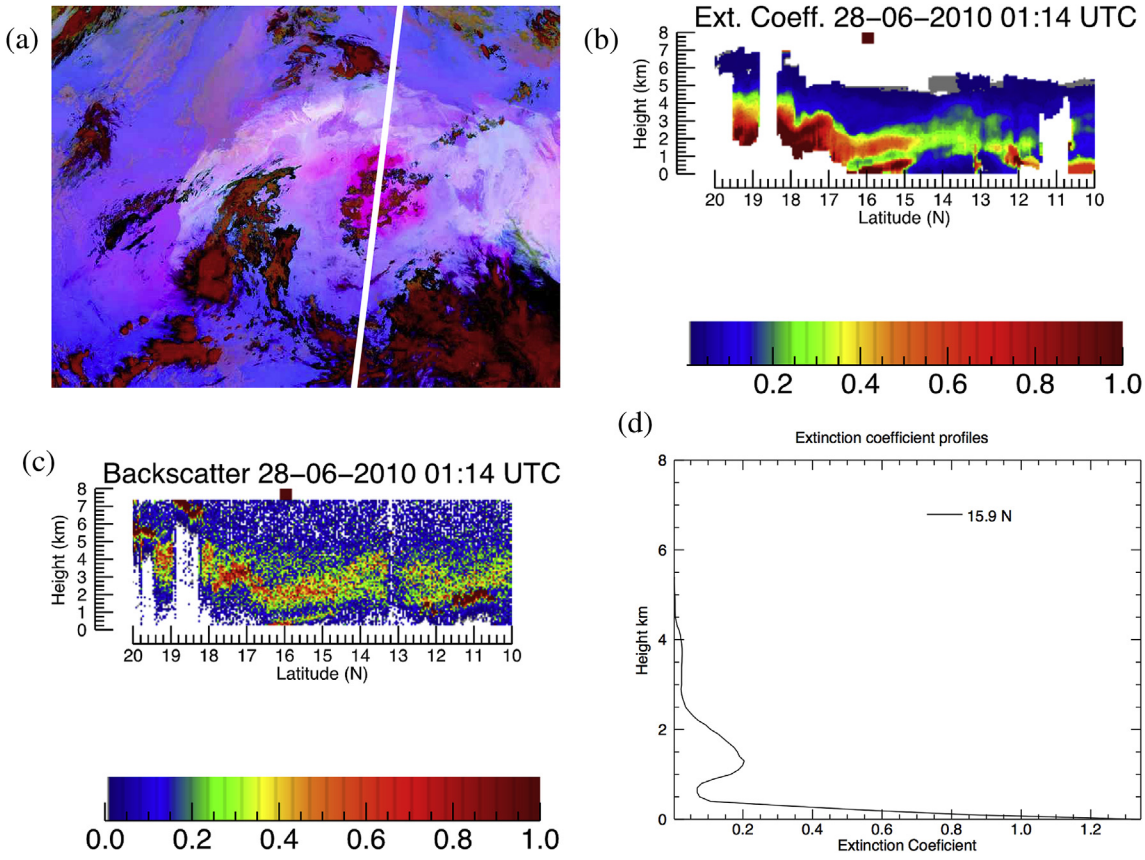

Fig. 6. As Fig. 4 but for 28th June 2010 at 01.15UTC.

monsoon flow (Karam et al., 2008).

A daytime Harmattan emission case over North-western Mali on 17th June 2011 is presented in Fig. 7. The dust plumes (Feature A in Fig. 7a) were generated by a LLJ emission event studied by (Ryder et al., 2013) and (Rosenberg et al., 2014). In this case the dust plume has been mixed almost to 2 km height as the daytime boundary layer developed (Fig. 7b,c). The emission algorithm identifies active emission at ~21 to 22°N (Fig. 7b) directly from the EC profile (Fig. 7d). Total lidar beam attenuation occurs in the near surface layers in the centre of the dust plume preventing dust emission identification, illustrating one of the sources of bias in the method.

4. Results and discussion

4.1. Spatial distribution of dust emission June–September 2006–2013

Over the eight year period 2006–13 inclusive, during JJAS the total number of cloud-free CALIOP observations (not shown) exceeds 2000 per 1.5° grid cell, providing at least 250 samples per grid box per season. The mean seasonal DEI map (Fig. 8a) shows a pattern of high dust emission over a broad zone of the central Sahara, extending over Southern Algeria, Northwest Niger and Northern Mali. Primary cores of emission maxima are located specifically over the Mali-Algerian border (Feature A at ~1°E, 21°N) and the Algeria–Niger border (Feature B at ~6°E, 19°N, extending south to ~3°E, 16°N). Relatively high DEI values are also observed over the following regions, in declining order of magnitude. (i) Western Mali-Eastern Mauritania centred ~19°N, 5°E (Feature C), with a hotspot near 22.5°N, 8°W. (ii) the Bodele depression in Northern Chad at ~17.5°N, 17.5°E and downwind (westward) thereof (Feature D). (iii) Eastern Niger centred ~16°N, 11°E (Feature E). (iv) Coastal Mauritania centred ~18°N, 15.5°E (Feature F). In addition, there appear some more localised features of high emission, notably; (i) The Southeast foothills of the Atlas Mountains close to the Algeria–Morocco border at 33°N, 2°E (Feature G). (ii) The Tidihelt depression near In Salah, Algeria at ~26°N, 1°E (Feature H). (iii) Extreme Northwest Mali at ~24°N, 5°W (Feature I).

This broad spatial pattern of dust emission shows a close correspondence with that of the SEVIRI DSA frequency of AW13 and S07 (Fig. 3a,b, respectively). Indeed, our analysis helps inform interpretation of some of the discrepancies in dust sources between the AW13 and S07 analyses. Specifically, we corroborate (i) the relative centre of gravity of DSA centred on the Mali–Algeria border region in AW13 (Fig. 3a matching closely with Feature A in Fig. 8a) compared to the relative DSA peak over Northern Mali in S07 (Fig. 3b) (ii) the relatively high emission activity over Eastern Mauritania evident in AW13 but less so in S07. Feature B in Fig. 8a corresponds closely with the 2nd most important region (after the Bodele Depression) of annual dust mass flux, estimated from integration of DSA and model flux estimates (Evan et al., 2015). The zone of maximum dust emission (Features A, B in Fig. 8a) is displaced significantly eastward (by ~7° eastward) with respect to the maximum MISR satellite AOT (Fig. 1). The relationship between the broad scale pattern and specific locations is discussed in Section 4.2 below.

The proportional frequency of emission (number of dust emission observations divided by the total number of non-cloud attenuated observations) indicates a maximum of ~0.1 over the zone of peak emission (Fig. 8b features A and B). This figure is close to equivalent values derived from the figures of AW13 and S07

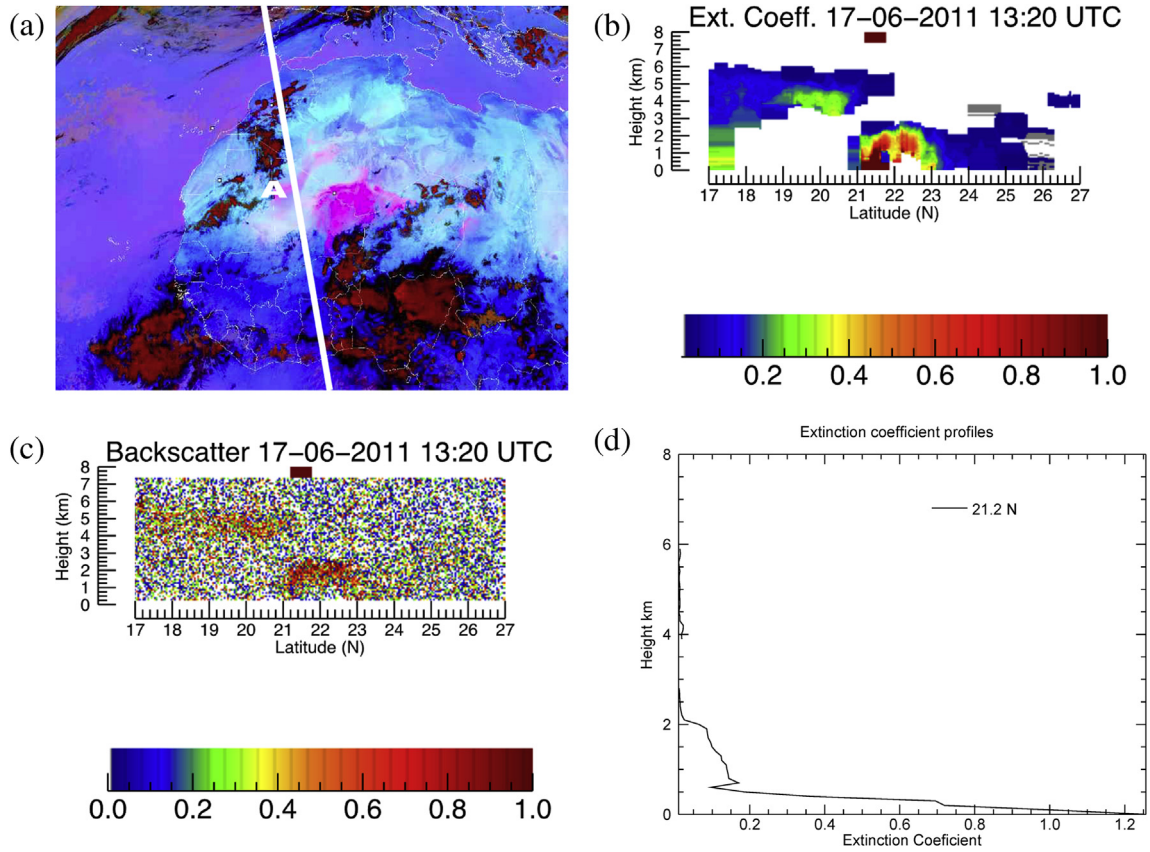

Fig. 7. As Fig. 4 but for 17th June 2011 at 13.15UTC.

(roughly estimated from DSA in Fig. 3 divided by the number of days, assuming a maximum of 1 dust plume per day per location in their analysis). A wide swath of the central Sahara extending eastward from Northern Mali through Southern Algeria to Western Niger experiences dust emission at least 4% of the time during summer.

Conversely, wide swathes of the Sahara desert experience little emission during the summer months, These regions include: (i) all the upland regions of North Africa including the Atlas, Hoggar, Tibesti and Air mountains. (ii) Most of Libya. (iii) Most of central and Northern Algeria excepting the specific sources noted above. (iv) Much of Eastern central Mauritania (iv) the Atlantic coastal regions north of ~22°N. This pattern corroborates that identified by S07 and AW13 and reinforces the extent to which vast swathes of the Sahara emit dust very infrequently.

Resolving the relative contributions of daytime and night-time emission is complicated by (i) smaller sample sizes leading to more noisy mean DEI fields (ii) differences in the performance of the retrieval algorithms between day and night due to the contrasting signal-noise ratio associated with the high solar background illumination during the day (Winker et al., 2013). Nevertheless, comparison of night-time and daytime DEI maps, normalised separately by their means (Fig. 8c), indicates that overall night-time relative dust emission is considerably higher (orange-red shading) over the core emission region of Northern Mali-Southern Algeria-Northern Niger (Features A and B in Fig. 8a). Notably, the night-time analysis shows greater emission in the more southern section of the core emission region in Eastern Mali (~3°E, 16°N) not highlighted in AW13 or S07.

4.2. Interpretation of the dust emission distribution

The summertime CWS dust zone, as identified from satellite AOT (Fig. 1) is a very large and ill-defined region of high column integrated dust loading. Our analysis and the recent DSA frequency maps of S07 and AW13 (Fig. 3) together provide a clear and consistent picture of dust emission occurring over a much more restricted region displaced to the east of the mean AOT maximum. We can further develop the previous explanations of this pattern as resulting from the interaction of surface geomorphological features, topography and climate.

The zone of maximum DEI over Northern Mali-Southern Algeria-Northwest Niger appears to be dominated by dust deflated primarily during night-time, thereby implicating convective cold pools as the likely dominant mechanism. This region lies to the northwest of a preferred locus of moist convection over northwest Niger (Laing et al., 2008; Mathon and Laurent, 2001) associated with the mean northward bulge in the inter-tropical discontinuity close to 0°E, and the lee of the Air Mountains. Thus, cold pool outflows from predominantly nocturnal convection over Western Niger propagate northwards into the Sahara driving *haboob* dust emission events identified in our analysis. These cold pool fronts are know to produce extreme surface wind speeds of ~15 to 20 ms^{-1} at 10 m height (Allen et al., 2013; Cuesta et al., 2010; Marsham et al., 2013), such that *Haboob* events may raise dust on many desert surfaces excluding bedrock. Dust emission is likely to peak when these systems travel over the more erodible fluvial (and palaeo-lacustrine) deposits, which are widespread on the Southern and Western flanks of these massifs (AW13). The DEI product is complementary to the DSA of AW13 and S07 in that DEI identifies

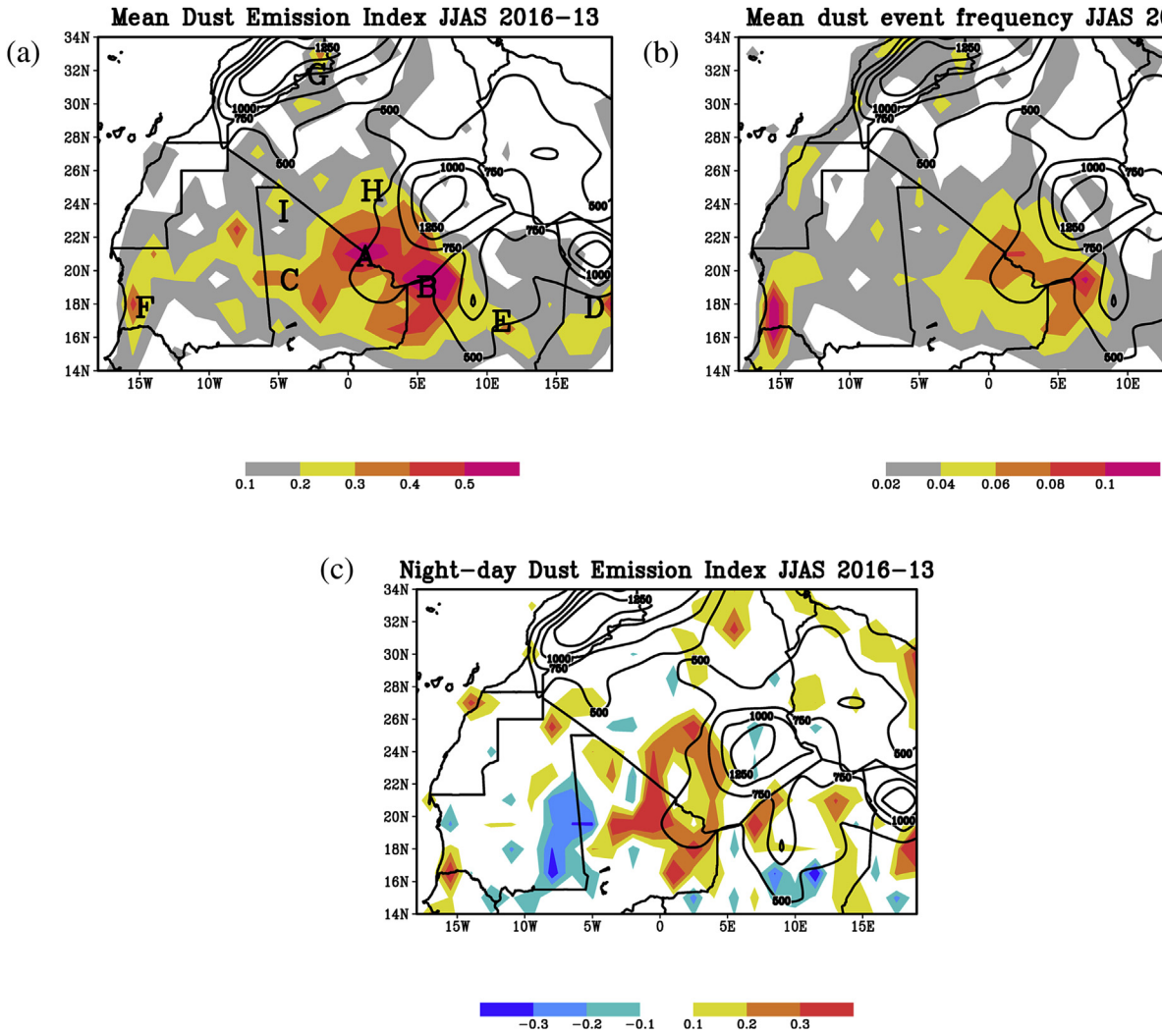

Fig. 8. Long-term mean dust emission quantities derived from our analysis for June–September 2006–13 on a 1.5-degree grid. (a) Mean dust emission intensity (DEI, shaded) (b) mean fractional emission (total counts as proportion of total cloud-free observations) (c) Mean night-time normalised DEI minus daytime normalised DEI. In each case contours indicate surface elevation at 500 m intervals.

active emission at any point in the dust plume lifespan, Evidence exists that *haboobs* invoke dust emission extensively during their propagation away from the MCS (where surface conditions allow) e.g. (Allen et al., 2013). The greater relative emission in the southern section (~3°E, 16°N) not highlighted in AW13 or S07 may be due to difficulties in the DSA method of back-tracking plumes close to convective cloud systems.

The DEI pattern in Fig. 8a bears remarkably close similarly to one of the two dominant patterns of high dustiness of (Ashpole and Washington, 2013a), that centred near the Algeria-Mali-Niger border triple point (TP) (rather than that featuring loadings to the west along the Mali–Algeria border, see their Fig. 2). (Ashpole and Washington, 2013a) note that this TP pattern is associated with monsoon surges towards the TP (with a eastward SHL locus), which will favour the night-time emission observed in our DEI maps, and that the TP centred pattern tends to precede by a few days the other westward-displaced pattern. Whilst this is consistent with westward propagating emission (perhaps linked to African Easterly Waves) it may also reflect westward transport of dust from the peak emission zone around the TP (which all the emission maps emphasise, Fig. 8a and Fig. 3), and is consistent with the eastward displacement of emission compared to column integrated dust loading.

In other regions the spatial pattern is consistent with the location of strongest winds and most erodible surface material. DEI maxima over Western Mali and Eastern Mauritania (Features C and I, respectively in Fig. 8a) and central Niger (Feature E in Fig. 8a) where daytime emission is preferred (blue shading in Fig. 8c), coincide with the preferred location of strong LLJs around the North-western and South-western flanks of the mean SHL position, respectively (see winds in Fig. 1). Similarly, the DEI maximum over the Bodele depression (Feature D Fig. 8a) coincides with strong mean LLJ winds through the Tibesti-Ennedi mountain gap.

Analysis of the DEI centres of activity in relation to surface topography (Fig. 8a) indicates a clear association (as with DSA from AW13 and S07). Dust emission occurs primarily in regions immediately to the south and southwest of the main Saharan mountains, namely the Hoggar, Adrar des Ifoghas, Air, Tibesti, and, to a lesser extent, the Atlas Mountains (see Fig. 1 for their locations). This is consistent with the very high resolution analysis of AW13 (and to a lesser extent S07) which indicates the existence of very localized specific source regions, mostly located in topographic depressions often with palaeo-lacustrine deposits or around the peripheries of mountains (notably the Hoggar and Air massifs, see Fig. 1 for

locations) where the specific sources are identified as outwash fluvial deposits. These features are small, ranging in size from a few tens to a few hundreds of km^2. Our analysis is, in part, consistent with this (compare Fig. 8a with Fig. 3a,b). Many of the isolated hotpots in our analysis do correspond with lacustrine depots including the paleolake deposits in the Tidihelt depression near In Salah, Algeria (Fig. 8a, Feature H), the Chott Ech Chergui in northwest Algeria (Fig. 8a, Feature G) and north of Erg Chech, Northern Mali (Fig. 8a, Feature I), although the low spatial resolution of our data binning procedure precludes definitive identification of sources at the scale of AW13. Overall, however, the DEI analysis indicates that substantial active emission occurs over a broad region of the central Sahara (A–B in Fig. 8a) in which the contribution to emission from such very localised specific preferential source regions remains uncertain. We infer that the strong winds in *haboob* events in particular may activate emission from desert surfaces of many types.

Despite the many similarities between the DEI and dust source activity from AW13 and S07, the DEI indicates stronger relative emission in the Southern Sahara/Sahel sectors of Mali and Niger between ~15 and 17°N. This may be due to more limited capacity of the SEVIRI product used in AW13 and S07 to detect dust at night and in more moist atmospheres, characteristic of the nocturnal monsoon flow influencing this region (Parker et al., 2005). Note the northward 'bulge' in the mean position of the ITD over Mali/Niger (Fig. 1). In this region emission, typically from cold pool events, will occur under conditions problematic for SEVIRI dust detection but less so for CALIOP. In addition, unlike DEI the analysis of S07 and AW13 are not scaled for the number of cloud-free observations, incurring a bias in total DSA towards cloud-free regions. Note that none of the satellite analyses can resolve dusts under cloud which (Kocha et al., 2013) infer can lead to an underestimate in AOT of up to 28% some locations.

With an active lidar instrument CALIOP has a uniquely powerful capability to observe aerosol processes at night. We find that night-time relative emission exceeds that during the daytime in the main core emission zone, with the caveat of a limited sampling of the full diurnal cycle. Whilst AW13 does not assess the diurnal timing of emission it is noted that (presumably nocturnal) convective cloud is associated with perhaps the dominant proportion of plumes in the zone approximately equivalent to A–B in Fig. 8a, consistent with our DEI diurnal analysis. This picture of substantial night-time emission is also consistent with field observations from Fennec (Marsham et al., 2013; Allen et al., 2013).

5. Summary, conclusions and caveats

We present results of a method to quantify dust emission over the remote central Sahara during the summertime based on analysis of vertical profiles of lidar extinction and backscatter from a long-term record of CALIOP satellite data. The method addresses some of the potential limitations of previous analysis, notably with the ability to detect dust emission at night and to derive an index of emission. The resulting maps of relative Dust Emission Index (DEI) indicate that in summertime dust emission is concentrated into a zone extending through Northern Mali, Southern Algeria and northwest Niger, on the southwest margins of the Hoggar and northwest margins of the Air mountains. The zone of maximum emission is displaced substantially eastward from the maximum of mean AOT. This broadly corroborates the analyses of AW13 and S07 and reinforces their inference that fluvial outwash deposits are an important source of erodible material. The convergence of evidence from independent sources is reassuring. Much of the Northern Sahara including Libya, Eastern Algeria experiences very little dust emission. Dust emission is higher at night than during day in contrast to the analysis of S07. Given the widespread in dust emission estimates in climate models (Fig. 2b) the results could be of value for model validation and development including potential scaling of emission in models to remove biases. The DEI distribution is potentially useful information to incorporate with soil and land cover surface boundary conditions in climate/weather model dust schemes (Cavazos et al., 2009).

A number of limitations of the method should be recognised. (i) As a profiling instrument with narrow swath the temporal sampling rate of CALIOP is fundamentally low. Despite the long (8-year) record providing reasonable sampling when integrated over a coarse grid there are inevitable sampling errors in observation of episodic dust emission events. The sampling errors will be highest where emission frequency is lowest. (ii) Retrieval of EC in the near surface layers is challenging and will be subject to, as yet unquantified, errors. The quality control screening which includes use of lidar backscatter profiles is designed to minimise these errors. As such due to the potential errors in the absolute EC estimates in near surface layers, the dependence of EC on dust size distribution and the absence of validation data, we suggest that the DEI should be considered an index of emission rather than a quantitative measure of dust emission. Whilst previous work has proposed a simple conversion of column AOT to dust mass (Koren et al., 2006) we do not suggest this is applicable to EC in the near surface layers. (iii) Although CALIOP's night-time capability samples the diurnal cycle much more fully than previous polar-orbiting sensors it provides only a partial sampling of the diurnal cycle, although the analysis of Kocha et al. (2013) suggest that the 13.30 and 01.30 local sampling times of CALIOP would represent well the diurnal cycle in AOT over the SHL region. (iv) Cases exist in which total attenuation of the lidar beam by heavy aerosol loading precludes emission detection. (v) Like other satellite methods the sensor cannot detect dust below cloud. (vi) The assumptions regarding the characteristic vertical profile of dust associated with active emission, which the algorithm uses to distinguish emission, is based on analysis of a relatively small number of case studies. However, extensive sensitivity analysis suggests the resulting DEI maps are robust to a wide range of values of thresholds used in the algorithm. However, the absence of systematic surface observations of dust emission in the Sahara means the DEI product cannot easily be independently validated. Despite reassuring convergence of evidence from independent SEVIRI and CALIOP analysis we suggest that multi-instrument approaches to dust emission quantification could be developed to overcome the limitations described above.

Acknowledgements

This work was funded under the NERC consortium grant ŒFennec: The Saharan Climate System[1] NE/G01826X/1.

Caliop data were obtained from the NASA Langley Research Center Atmospheric Science Data Center.

References

Allen, C.J.T., Washington, R., Engelstaedter, S., 2013. Dust emission and transport mechanisms in the central Sahara: fennec ground-based observations from Bordj Badji Mokhtar, June 2011. J. Geophys. Res. Atmos. 118 (12), 6212–6232.

Ashpole, I., Washington, R., 2012. An automated dust detection using SEVIRI: a multiyear climatology of summertime dustiness in the central and western Sahara. J. Geophys. Res. Atmos. 117.

Ashpole, I., Washington, R., 2013a. Intraseasonal variability and atmospheric controls on daily dust occurrence frequency over the central and western Sahara during the boreal summer. J. Geophys. Res. Atmos. 118 (23), 12915–12926.

Ashpole, I., Washington, R., 2013b. A new high-resolution central and western Saharan summertime dust source map from automated satellite dust plume tracking. J. Geophys. Res. Atmos. 118 (13), 6981–6995.

Banks, J.R., et al., 2013. Intercomparison of satellite dust retrieval products over the west African Sahara during the Fennec campaign in June 2011. Remote Sens.

Environ. 136, 99–116.
Brindley, H., Knippertz, P., Ryder, C., Ashpole, I., 2012. A critical evaluation of the ability of the spinning enhanced visible and infrared imager (SEVIRI) thermal infrared red-green-blue rendering to identify dust events: theoretical analysis. J. Geophys. Res. Atmos. 117.
Cavazos, C., Todd, M.C., Schepanski, K., 2009. Numerical model simulation of the Saharan dust event of 6-11 March 2006 using the regional climate model version 3 (RegCM3). J. Geophys. Res. Atmos. 114.
Chen, B., et al., 2010. Detection of dust aerosol by combining CALIPSO active lidar and passive IIR measurements. Atmos. Chem. Phys. 10 (9), 4241–4251.
Chiapello, I., Moulin, C., 2002. TOMS and METEOSAT satellite records of the variability of Saharan dust transport over the Atlantic during the last two decades (1979-1997). Geophys. Res. Lett. 29 (8).
Cuesta, J., Lavaysse, C., Flamant, C., Mimouni, M., Knippertz, P., 2010. Northward bursts of the West African monsoon leading to rainfall over the Hoggar Massif, Algeria. Q. J. R. Meteorol. Soc. 136, 174–189.
Emmel, C., Knippertz, P., Schulz, O., 2010. Climatology of convective density currents in the southern foothills of the Atlas Mountains. J. Geophys. Res. Atmos. 115.
Evan, A.T., et al., 2015. Derivation of an observation-based map of North African dust emission. Aeolian Res. 16, 153–162.
Fiedler, S., Schepanski, K., Heinold, B., Knippertz, P., Tegen, I., 2013. Climatology of nocturnal low-level jets over North Africa and implications for modeling mineral dust emission. J. Geophys. Res. Atmos. 118 (12), 6100–6121.
Flamant, C., et al., 2009. The impact of a mesoscale convective system cold pool on the northward propagation of the intertropical discontinuity over West Africa. Q. J. R. Meteorol. Soc. 135 (638), 139–159.
Forster, P., et al., 2007. Changes in Atmospheric Constituents and in Radiative Forcing. In: Climate Change 2007: the Physical Science Basis. Contribution of Working Group I to the Fourth Assessment Report of the Intergovernmental Panel on Climate Change. Cambridge University Press, Cambridge, United Kingdom; New York, NY, USA.
Ginoux, P., et al., 2001. Sources and distributions of dust aerosols simulated with the GOCART model. J. Geophys. Res. Atmos. 106 (D17), 20255–20273.
Jickells, T.D., et al., 2005. Global iron connections between desert dust, ocean biogeochemistry, and climate. Science 308 (5718), 67–71.
Karam, D.B., et al., 2008. Dust emissions over the Sahel associated with the West African monsoon intertropical discontinuity region: a representative case-study. Q. J. R. Meteorol. Soc. 134 (632), 621–634.
Knippertz, P., Todd, M.C., 2010. The central west Saharan dust hot spot and its relation to African easterly waves and extratropical disturbances. J. Geophys. Res. Atmos. 115.
Kocha, C., Tulet, P., Lafore, J.P., Flamant, C., 2013. The importance of the diurnal cycle of aerosol optical depth in West Africa. Geophys. Res. Lett. 40 (4), 785–790.
Koren, I., et al., 2006. The Bod,l, depression: a single spot in the Sahara that provides most of the mineral dust to the Amazon forest. Environ. Res. Lett. 014005, doi: 10.1088/1748-9326/1/1/014005.
Laing, A.G., Carbone, R., Levizzani, V., Tuttle, J., 2008. The propagation and diurnal cycles of deep convection in northern tropical Africa. Q. J. R. Meteorol. Soc. 134 (630), 93–109.
Lavaysse, C., et al., 2009. Seasonal evolution of the West African heat low: a climatological perspective. Clim. Dyn. 33 (2–3), 313–330.
Lensky, I.M., Rosenfeld, D., 2008. Clouds-aerosols-precipitation satellite analysis tool (CAPSAT). Atmos. Chem. Phys. 8 (22), 6739–6753.
Liu, Z., et al., 2009. The CALIPSO lidar cloud and aerosol discrimination: version 2 algorithm and initial assessment of performance. J. Atmos. Ocean. Technol. 26 (7), 1198–1213.
Mahowald, N.M., et al., 2010. Observed 20th century desert dust variability: impact on climate and biogeochemistry. Atmos. Chem. Phys. 10 (22), 10875–10893.
Marsham, J.H., et al., 2013. Meteorology and dust in the central Sahara: observations from Fennec supersite-1 during the June 2011 intensive observation period. J. Geophys. Res. Atmos. 118 (10), 4069–4089.
Mathon, V., Laurent, H., 2001. Life cycle of Sahelian mesoscale convective cloud systems. Q. J. R. Meteorol. Soc. 127 (572), 377–406.
Parker, D.J., et al., 2005. The diurnal cycle of the West African monsoon circulation. Q. J. R. Meteorol. Soc. 131 (611), 2839–2860.
Peyridieu, S., et al., 2013. Characterisation of dust aerosols in the infrared from IASI and comparison with PARASOL, MODIS, MISR, CALIOP, and AERONET observations. Atmos. Chem. Phys. 13 (12), 6065–6082.
Prospero, J.M., Ginoux, P., Torres, O., Nicholson, S.E., Gill, T.E., 2002. Environmental characterization of global sources of atmospheric soil dust identified with the Nimbus 7 total ozone mapping spectrometer (TOMS) absorbing aerosol product. Rev. Geophys. 40 (1).
Ridley, D.A., Heald, C.L., Ford, B., 2012. North African dust export and deposition: a satellite and model perspective. J. Geophys. Res. Atmos. 117.
Rosenberg, P.D., et al., 2014. Quantifying particle size and turbulent scale dependence of dust flux in the Sahara using aircraft measurements. J. Geophys. Res. Atmos. 119 (12), 7577–7598.
Ryder, C.L., et al., 2013. Optical properties of Saharan dust aerosol and contribution from the coarse mode as measured during the Fennec 2011 aircraft campaign. Atmos. Chem. Phys. 13 (1), 303–325.
Schepanski, K., Tegen, I., Laurent, B., Heinold, B., Macke, A., 2007. A new Saharan dust source activation frequency map derived from MSG-SEVIRI IR-channels. Geophys. Res. Lett. 34 (18).
Schepanski, K., Tegen, I., Macke, A., 2012. Comparison of satellite based observations of Saharan dust source areas. Remote Sens. Environ. 123, 90–97.
Schepanski, K., et al., 2009. Meteorological processes forcing Saharan dust emission inferred from MSG-SEVIRI observations of subdaily dust source activation and numerical models. J. Geophys. Res. Atmos. 114.
Tegen, I., et al., 2002. Impact of vegetation and preferential source areas on global dust aerosol: results from a model study. J. Geophys. Res. Atmos. 107 (D21).
Textor, C., et al., 2007. The effect of harmonized emissions on aerosol properties in global models - an AeroCom experiment. Atmos. Chem. Phys. 7 (17), 4489–4501.
Todd, M.C., et al., 2013. Meteorological and dust aerosol conditions over the western Saharan region observed at Fennec Supersite-2 during the intensive observation period in June 2011. J. Geophys. Res. Atmos. 118 (15), 8426–8447.
Todd, M.C., et al., 2008. Quantifying uncertainty in estimates of mineral dust flux: an intercomparison of model performance over the Bodele Depression, northern Chad. J. Geophys. Res. Atmos. 113.
Vaughan, M., et al., 2004. Fully automated analysis of space-based lidar data: an overview of the CALIPSO retrieval algorithms and data products. Proc. SPIE 5575, 16–30.
Washington, R., Todd, M., Middleton, N.J., Goudie, A.S., 2003. Dust-storm source areas determined by the total ozone monitoring spectrometer and surface observations. Ann. Assoc. Am. Geogr. 93 (2), 297–313.
Washington, R., Todd, M.C., Engelstaedter, S., Mbainayel, S., Mitchell, F., 2006. Dust and the low-level circulation over the Bodele Depression, Chad: observations from BoDEx 2005. J. Geophys. Res. Atmos. 111 (D3).
Williams, E., et al., 2009. The electrification of dust-lofting gust fronts ('haboobs') in the Sahel. Atmos. Res. 91 (2–4), 292–298.
Winker, D.M., et al., 2010. The CALIPSO mission a global 3D view of aerosols and clouds. Bull. Am. Meteorol. Soc. 91 (9), 1211–1229.
Winker, D.M., et al., 2013. The global 3-D distribution of tropospheric aerosols as characterized by CALIOP. Atmos. Chem. Phys. 13 (6), 3345–3361.
Winker, D.M., et al., 2009. Overview of the CALIPSO mission and CALIOP data processing algorithms. J. Atmos. Ocean. Technol. 26 (11), 2310–2323.
Young, S.A., Vaughan, M.A., 2009. The retrieval of profiles of particulate extinction from cloud-aerosol lidar infrared pathfinder satellite observations (CALIPSO) data: algorithm description. J. Atmos. Ocean. Technol. 26 (6), 1105–1119.